Measurement of Interfacial Thermal Resistance at Microstructured Si-water Interface Using Steady State Method

Yu, Yankun
Graduate School of Engineering, Kyushu Institute of Technology

Nagayama, Gyoko
Department of Mechanical Engineering, Kyushu Institute of Technology

https://doi.org/10.5109/5909104

出版情報：Proceedings of International Exchange and Innovation Conference on Engineering & Sciences (IEICES). 8, pp.278-284, 2022-10-20. Interdisciplinary Graduate School of Engineering Sciences, Kyushu University
バージョン：

Proceedings of the 8th International Exchange and Innovation Conference on Engineering & Sciences (IEICES 2022)

Measurement of Interfacial Thermal Resistance at Microstructured Si–water Interface Using Steady State Method

Yankun Yu[1], Gyoko Nagayama[2*]
[1]Graduate School of Engineering, Kyushu Institute of Technology, Kitakyushu, Fukuoka 804-8550, Japan
[2]Department of Mechanical Engineering, Kyushu Institute of Technology, Kitakyushu, Fukuoka 804-8550, Japan
*Corresponding author email: nagayama.gyoko725@mail.kyutech.jp

Abstract: *Interfacial thermal resistance at solid–liquid interface is of great importance for thermal design of electronic devices. However, the quantitative investigation of interfacial thermal resistance is still open for question. In this study, the steady state method based on ASTM-5470 standard was applied to measure the interfacial thermal resistance at the microstructured Si–water interface. The effects of microstructure geometrical parameters on surface wettability and interfacial thermal resistance were studied. The experimental interfacial thermal resistance at the microstructured Si-water interface shows a dependence on the microstructure geometrical parameters, in correspondence with the surface wetting based on the intermediate wetting state theory.*

Keywords: Interfacial thermal resistance, Steady state method, Solid–liquid interface, Wettability, Microstructured surface

1. INTRODUCTION

Thermal transport across solid–liquid interfaces has gained significant importance due to the vast applications of thermal interface materials in numerous important engineering fields including electronic packaging, aerospace technology, optoelectronic devices, metal working industries, cryogenics, automotive manufacturing and so on [1–4]. Of all the interfacial properties, interfacial thermal resistance is a key parameter to characterize heat transfer performance across solid–liquid interfaces for thermal management.

Any surface which appears to be smooth at macro scale has grooves and cavities at the microscopic level. If a liquid comes into contact with a solid, it spreads out and wets the solid surface. However, microgrooves and microcavities can induced unwetted area, which causes temperature drop at the solid–liquid interface when a heat flow goes through the solid–liquid interface. The poor contact between solid and liquid at the solid–liquid interface results in the so-called interfacial thermal resistance.

The interfacial thermal resistance originates from the observation by Kapitza [5] in 1941. A temperature discontinuity was found at the boundary between copper and liquid helium while a heat flux was passing through the interface. So far, the interfacial thermal resistance has been extensively studied using both theoretical models [6–17] and experimental methods [18–28].

Relevant theoretical models for the solid–liquid interfacial thermal resistance have been established based on the surface morphology and solid–liquid contact mechanisms. Thus, the factors of solid–liquid interfacial thermal resistance remain complex due to the complexity stems from the surface morphology description. Also, the wettability of the liquid on the rough surface must be considered in the theoretical models because the thermal transport across the solid−liquid interface is affected by the affinity between the phases (wettability), and those properties of liquid and solid.

To describe the static contact angle of liquid at the structured solid surface, three kinds of wetting states have been developed. The Wenzel model [29] represents the fully wetted state, the Cassie-Baxter model [30] indicates the non-wetted state, while a partial wetting model [31] describes an intermediate state between the Wenzel and Cassie-Baxter states. Since the different wetting states induce different solid–liquid contact area between solid and liquid, the thermal contact resistance at the solid–liquid interface relates to the wetting state.

Extensive experimental techniques for characterizing the interfacial thermal resistance or thermal boundary/ contact resistance have been proposed [32–36]. Two typical techniques are usually applied to measure the thermal resistance: steady-state method and transient method, according to whether the temperature varies with time. The steady-state method is usually conducted based on the American Society for Testing and Materials 5470 (ASTM-5470) [32]. The transient methods include the infrared thermography measurement [33], the 3ω method [34], the laser-flash measurement [35-36], the time-domain thermoreflectance measurement [37-40], and the photoacoustic techniques [41], etc. The advantages of these transient methods are their non-intrusive detection, short measurement time, and rapid response. But their measurement accuracy is comparatively unsatisfactory since their theoretical derivation is complicated and includes many influencing factors. Compared to the transient methods, the steady state methods provide better measurement accuracy, although this takes longer to achieve. However, limitations to the samples exit and it’s still a challenge to measure the interfacial thermal resistance at the Si-water solid–liquid interfaces.

In this study, a steady state method based on ASTM-5470 standard was used to measure the interfacial thermal resistance at the microstructured Si–water interface. Microstructured Si surfaces with varied geometrical parameters were designed and fabricated by deep reactive-ion etching method. The wettability at the microstructured Si–water interface was characterized by water contact angle measurements. A comprehensive analysis was carried out to clarify the relationship of wettability and solid–liquid interfacial thermal resistance.

2. MATERIALS AND METHODS

2.1 Sample fabrication

To prepare microstructured Si surfaces, P-type (100) Si wafers with size of 15 mm × 15 mm were cleaned using acetone, isopropanol, and pure water for 10 minutes at

180°C sequentially. The cleaned Si wafers were deposited with a photoresist and then patterned using a maskless lithography (NEOARK, DDB-701-MS). After the application of the photoresist, square pore micro-patterns over an area of 8 mm × 8 mm were developed through a deep reactive-ion etching apparatus (SAMCO, RIE-400iPB). The remaining photoresist was removed by O_2 plasma treatment for 30 seconds followed by acetone immersion.

A scanning electron microscope image of the microstructured Si surface is shown in Fig. 1. The microstructure part consists of uniform arranged rectangular holes with size *a*, distance between holes *b* and depth *h*.

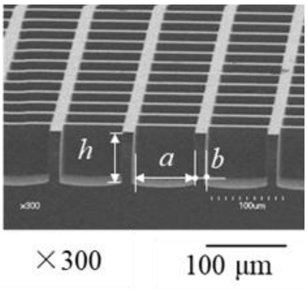

Fig. 1. A scanning electron microscope image of the microstructured Si surface when h = 12 μm, a = 80 μm, and b = 20 μm.

As shown in Table 1, all the microstructured Si samples are divided into two groups according to hole depth *h* (12 μm and 40 μm, respectively). In each group, there are 5 samples with same distance between two square holes *b* = 20 μm, and different hole size *a* varying from 12 μm to 380 μm. Three dimensionless parameters (the solid fraction Φ, surface area increment ratio r_w and effective wetting ratio *f*) according to the partial wetting model are calculated to predict the theoretical contact angles at different wetting states, as shown below.

$$\Phi = \frac{(a+b)^2 - a^2}{(a+b)^2} \tag{1}$$

$$r_w = \frac{(a+b)^2 + 4ah}{(a+b)^2} \tag{2}$$

$$f = 1 - \Phi^{D-2} \tag{3}$$

where D = 2.4 is the fractal dimension.

2.2 Contact angle measurement

The water contact angle measurement was conducted in a room under constant temperature and moisture at 20°C, 40% relative humidity. Four μL deionized water droplet was dropped on the Si surfaces using a micro syringe, and its image was recorded by a digital microscope (Keyence, VHX-200). Six static water contact angle measurements were performed on different spots all over the pattern area at sample surface. Before water contact angle measurements, all the Si samples were cleaned in an ultrasonic bath for 10 mins using acetone, isopropyl alcohol, and deionized water.

Table 1. Parameters of microstructured Si surfaces.

h [μm]	a [μm]	b [μm]	Φ	r_w	f
12	12	20	0.85	1.59	0.04
	30	20	0.64	1.59	0.10
	80	20	0.37	1.39	0.21
	230	20	0.16	1.18	0.35
	380	20	0.11	1.12	0.41
40	12	20	0.86	2.94	0.04
	30	20	0.63	2.98	0.11
	80	20	0.36	2.31	0.22
	230	20	0.16	1.60	0.36
	380	20	0.11	1.39	0.42

2.3 Interfacial thermal resistance measurement

The schematic of the experimental setup is shown in Fig. 2.

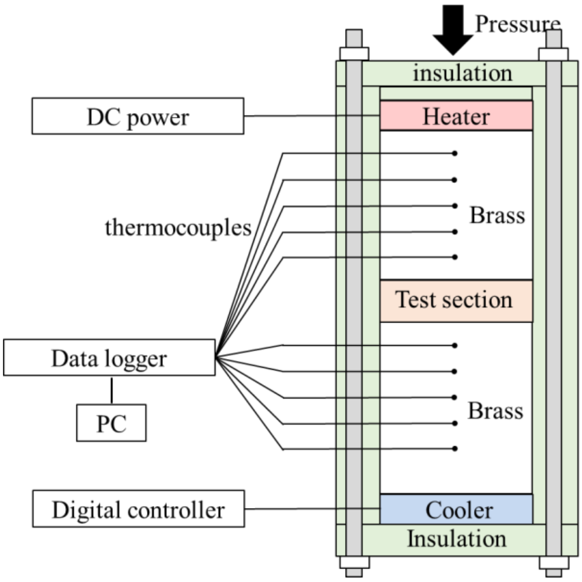

Fig. 2. Schematic of experimental setup based on ASTM-5470 standard.

The experimental system consists of a heater, a cooler, a test section, two brass (Br) bars, a data acquisition system, insulation, and a pressure loading unit. The heater is powered by a regulated DC power supply (PK 120-3.3, Matsusada, Japan) and its size is 15 mm ×15 mm ×1.27 mm. The cooler is controlled by a thermomoulded digital controller (SPE-UC-100, SAKAGUCHI, Japan). The Br bars between the heater and cooler have the cross-section area of 15 mm × 15 mm and its thermal conductivity λ_{Br} has been confirmed to be 109 W/(m · K) using ten T-type thermocouples buried in the Br bars. The data acquisition system is applied to collect the temperatures measured by the thermocouples using a datalogger (GL840-SDWV, GRAPHTEC, Japan). Since the interfacial thermal resistance is sensitive to the pressure, the pressure loading unit is implemented by a fixed weight and the pressure applied to all samples is 0.11 MPa.

The fabricated samples (see section 2.1) are installed into the test section and sandwiched between the two Br bars. To measure the solid–liquid interfacial thermal resistance between Si surface and water, a soft silicon film of 15 mm × 15 mm × 0.5 mm was used to separate Si samples, with a hole of 8 mm × 8 mm cut in the center of the film as a thin tank for water layer.

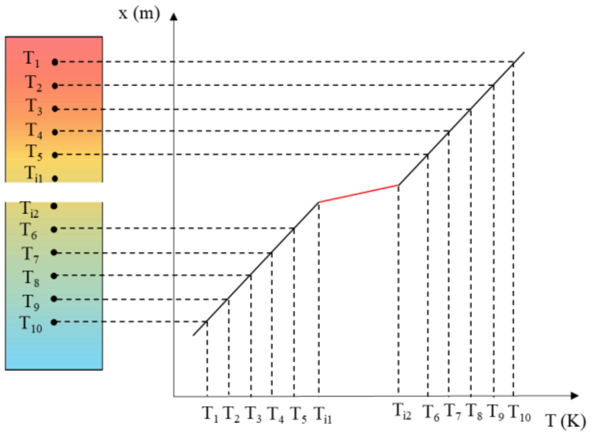

Fig. 3. Schematic of the temperature profile in the Br bars under a steady state.

A schematic of the temperature profile in the Br bars is shown in Fig. 3 based on ASTM D5470 method. When the experimental system reaches a steady state, the heat flux can be obtained by the temperature gradient and thermal conductivity of the Br. From the Fourier law, the heat flux q of each Br bar is,

$$q_1 = -\lambda_{Br}\left(\frac{dT}{dx}\right)_1 \qquad (4)$$

$$q_2 = -\lambda_{Br}\left(\frac{dT}{dx}\right)_2 \qquad (5)$$

where dT/dx is the temperature gradient of the Br bar. Subscripts 1 and 2 indicate the top and bottom bars respectively. The average heat flux q is obtained as follows.

$$q = \frac{q_1 + q_2}{2} \qquad (6)$$

The temperatures at the Br-Si contact surface T_{i1}, T_{i2} can be obtained by extrapolating from the temperature gradient. The temperature difference between T_{i1} and T_{i2} becomes

$$\Delta T = T_{i1} - T_{i2} \qquad (7)$$

Therefore, the overall thermal resistance of the test section can be calculated.

$$R = \frac{\Delta T}{q} \qquad (8)$$

As shown in Fig. 4, four experimental measurements were designed to obtain all the thermal resistance parameters. The thermal resistance of the path through the silicon film R_1 is the summation of the thermal resistance of the silicon film R_{film} and the thermal resistance between the Si surface and the silicon film $R_{Si-film}$.

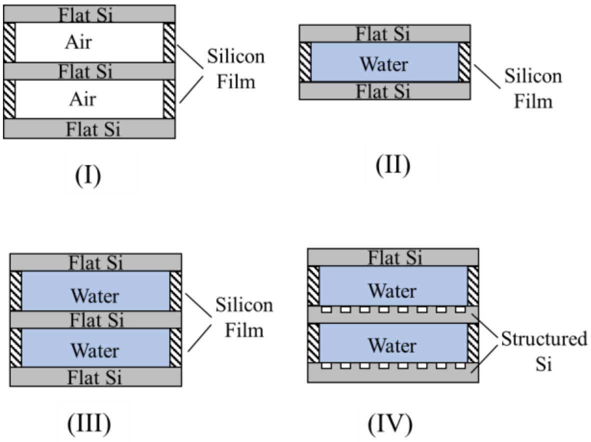

Fig. 4. Measurement method of solid–liquid interfacial thermal resistance.

$$R_1 = R_{film} + 2R_{Si-film} \qquad (9)$$

The thermal resistance of the path through the flat Si and water contact area shown in Fig. 3 (II) and (III) is

$$R_2 = 2R_i + R_{water} \qquad (10)$$

where R_{water} is the thermal resistance of the water layer and R_i is the interfacial thermal resistance between flat Si surface and water.

For the microstructured Si surface as shown in Fig. 3 (IV), the thermal resistance of the path through the Si and water contact area is

$$R_2' = R_i + R_{water} + R_i' \qquad (11)$$

here R_i' is the interfacial thermal resistance between microstructured Si surface and water.

Therefore, the overall thermal resistances for the four measurements can be summarized as follows.

$$R_{\mathrm{I}} = 2R_{Si-Br} + 3R_{Si} + 2R_1 \qquad (12)$$

$$R_{\mathrm{II}} = 2R_{Si-Br} + 2R_{Si} + \frac{1}{\frac{1}{R_1} + \frac{1}{R_2}} \qquad (13)$$

$$R_{\mathrm{III}} = 2R_{Si-Br} + 3R_{Si} + \frac{2}{\frac{1}{R_1} + \frac{1}{R_2}} \qquad (14)$$

$$R_{\mathrm{IV}}=2R_{Si-Br}+3R_{Si}+\frac{2}{\frac{1}{R_1}+\frac{1}{R_2'}} \qquad (15)$$

where R_{Si-Br} the thermal contact resistance between the Si surface and the Br surface, R_{Si} is the thermal resistance of the Si sample.

Since the thermal resistance of bulk materials is the ratio of material thickness δ to its thermal conductivity λ, the thermal resistance of Si and water result in

$$R_{Si}=\frac{\delta_{Si}}{\lambda_{Si}} \qquad (16)$$

and

$$R_{water}=\frac{\delta_{water}}{\lambda_{water}} \qquad (17)$$

Combining Eqs. 12-14 and 16-17, R_{Si-Br} and R_1 can be obtained by:

$$R_{Si-Br}=\frac{2R_{\mathrm{II}}-R_{\mathrm{III}}-R_{Si}}{2} \qquad (18)$$

and

$$R_1=\frac{R_{\mathrm{I}}-2R_{Si-Br}-3R_{Si}}{2} \qquad (19)$$

Thus, the interfacial thermal resistance R_i and R_i' can be expressed as:

$$R_i=\frac{1}{\frac{1}{R_{\mathrm{III}}-2R_{Si-Br}-3R_{Si}}-\frac{2}{R_1}}-\frac{R_{water}}{2} \qquad (20)$$

$$R_i'=\frac{1}{\frac{2}{R_{\mathrm{IV}}-2R_{Si-Br}-3R_{Si}}-\frac{1}{R_1}}-R_{water}-R_i \qquad (21)$$

3. RESULTS AND DISCUSSION

3.1 Wettability analysis

Figure 5 shows the measured contact angle of the microstructured Si as a function of hole size. The dotted black line represents the dividing line of hydrophilicity and hydrophobicity. When the hole size *a* increases, the contact angle gradually increases and the original hydrophilic surface changes to a hydrophobic surface. When *a* is smaller than 60 μm, microstructured Si surfaces appear hydrophilic and, in any case, hydrophobic. This change in wettability can be found through the microscopic images of the droplet on the sample surfaces as shown in Fig. 6.

In addition, the measured contact angle shows the largest gap at minimum hole size *a*=12 μm. As the hole size a increases, the variation in the wettability of micro-structured Si surfaces due to hole depth *h* on becomes negligible.

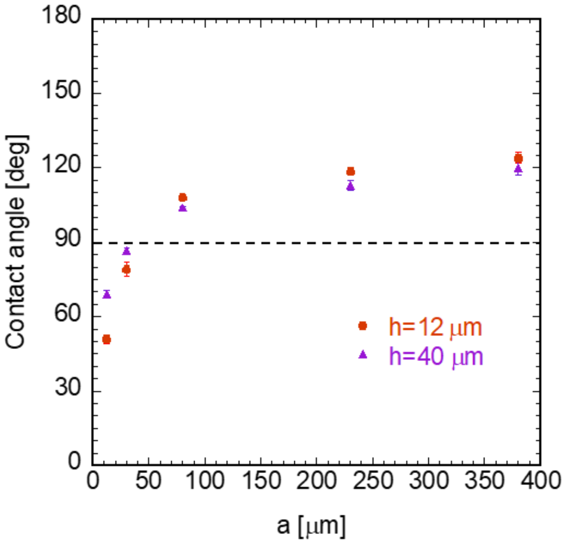

Fig. 5. Experimental water contact angle results as a function of hole size *a*.

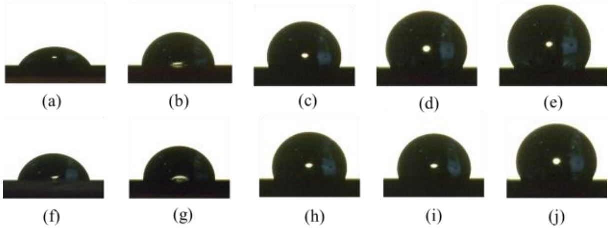

Fig. 6. Microscope images of 4 μL water droplet on microstructured Si surfaces. (a) ~ (e): *h* = 12 μm; (f) ~ (j): *h* = 40 μm.

The theoretical wettability analysis was conducted based on the partial wetting model, in which the effective wetting ratio *f* was defined to the proportion of liquid wetting into the structure. The wetting state is Wenzel state when *f* is 0, Cassie−Baxter state when *f* is 1, and intermediate wetting state when 0<*f*<1, respectively. The predicted contact angles of Cassie-Baxter model (θ_C), partial wetting model (θ_P) and Wenzel model (θ_W) can be expressed by following equations:

$$\cos\theta_C=\Phi\cos\theta_Y+(1-\Phi)\cos 180^{\circ} \qquad (22)$$

$$\cos\theta_W=r_w\cos\theta_Y \qquad (23)$$

$$\cos\theta_P=[\Phi+(r_w-\Phi)f]\cos\theta_Y + [(1-\Phi)(1-f)]\cos 180^{\circ} \qquad (24)$$

The experimental results are compared with the corresponding theoretical results at three wetting states, as shown in Figs. 7 and 8.

When *h* =12 μm and *a*≤80 μm, the experimental results show good agreement with that of Cassie-Baxter model and increase towards a trend between Cassie-Baxter model and partial wetting model. As the hole size increases, the ability of surface tension to support water diminishes, resulting into the water gradually wetting the hole. This difference in the wetting ratio of the microstructure manifests itself as a difference in the wetting state of the structured surface at the macroscopic scale. The similar phenomenon is also found in Fig. 8. However, the difference is when h =40 µm, the experimental contact angle does not match Cassie-Baxter model as h =12 µm.

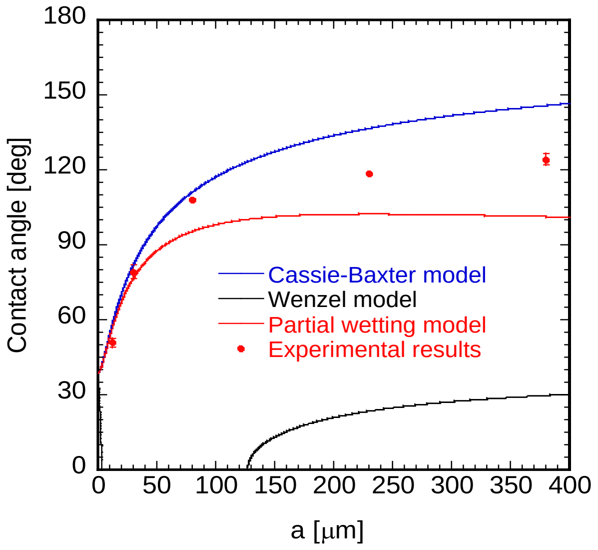

Fig. 7. Theoretical and experimental contact angles on microstructured Si surfaces with hole depth h =12 µm.

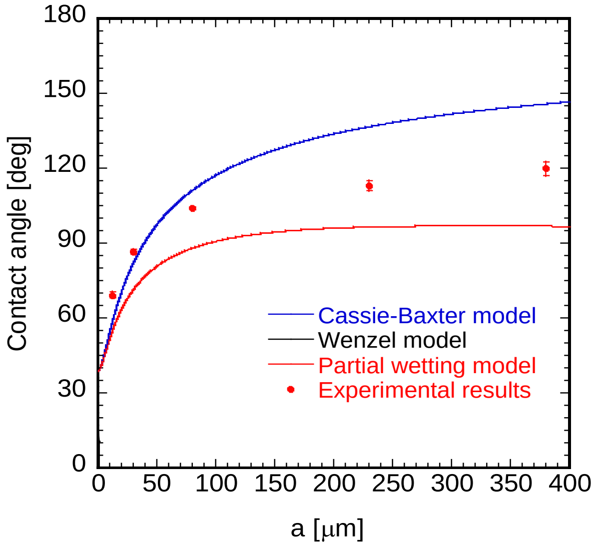

Fig. 8. Theoretical and experimental contact angles on microstructured Si surfaces with hole depth h =40 µm.

3.2 Interfacial thermal resistance analysis

The experimental results of interfacial thermal resistance at microstructured Si–water interface is shown in Fig. 9. With the increase of hole size, the solid–liquid interfacial thermal resistance shows a curve with its maximum value at a = 80 µm and 230 µm, respectively. The trend in interfacial thermal resistance can be explained by the changes in the wettability at microstructured Si surface. When the hole size is very small and the wetting state is Cassie-Baxter state, the holes of the microstructured Si surface are non-wetted. At this point, as a increases, the contact angle increases, the surface of the structure becomes more hydrophobic and the contact area of the solid-liquid interface decreases, leading to an increase in the solid–liquid interfacial thermal resistance. As a continues to increase, the wetting state changes from the Cassie-Baxter state to the partial wetting state, and water begins to enter the holes. In this case, the synergy of contact angle and wetting state determines the solid-liquid interfacial contact area, i.e., the solid–liquid interfacial thermal resistance.

When h =12 µm, the maximum of thermal resistance appears at a =80 µm, which coincides with the wetting state transition point in Fig. 7. The interfacial thermal resistance is dominated by the real wetting state in this instance. When $a \leq 80$ µm, the structured Si surface agrees with Cassie-Baxter model, indicating that the surface is in a non-wetted state. As therefore the air gap trapped between structure and water increases when hole size increases, resulting in an increasing interfacial thermal resistance. When $a > 80$ µm, the wetting state lies between non-wetted state and intermediate wetting state, which indicates that water begins to enter the structure and the air layer is reduced, resulting in a decrease in thermal resistance at the interface.

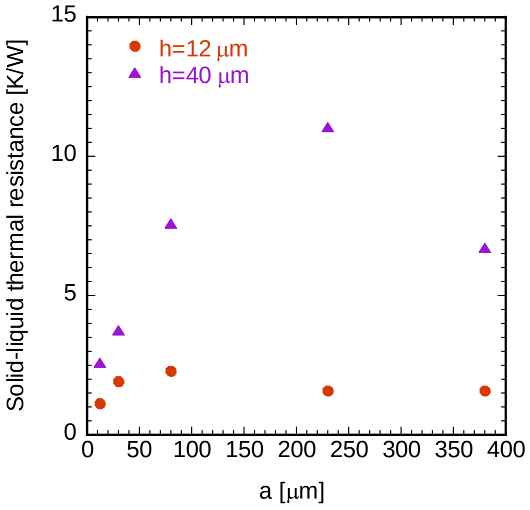

Fig. 9. Interfacial thermal resistance at microstructured Si–water interface as a function of hole size a.

It is clear that when h = 40 µm, the solid–liquid interfacial thermal resistance increases steadily as hole size a increases, and begins to drop at the maximum a value. Although it shows a similar turning point with the case of h =12 µm in Fig. 8, the reduction in air gap by the change in wetting state is not discernible at a smaller hole size since it is four times deeper than the samples with depth of 12 µm. The difference in interfacial thermal resistance for the same hole size also demonstrates that variations in air gap are the primary cause of interfacial thermal resistance variances.

4. CONCLUSION

In this study, a steady state method based on ASTM-5470 standard was used to measure the interfacial thermal resistance at the microstructured Si–water interface. The experimental interfacial thermal resistance at the microstructured Si-water interface shows a dependence on the microstructure geometrical parameters, in correspondence with the surface wetting based on the intermediate wetting state theory. A comprehensive analysis was carried out to clarify the relationship of wettability and solid–liquid interfacial thermal resistance. The results show that the interfacial thermal resistance is determined by the synergy of contact angle and wetting state at microstructured Si surfaces.

5. REFERENCES

[1] M. Grujicic, C.L. Zhao, E.C. Dusel, The effect of thermal contact resistance on heat management in the electronic packaging, 246 (2005) 290–302.

[2] S. Ghosh, S. Harish, Bidyut Baran Saha, Electrical Power Estimation of Thermoelectric Cement Composites with Inclusion of Nanostructured Materials, Proceedings of International Exchange and Innovation Conference on Engineering & Sciences (IEICES). 6 (2020) 27–33.

[3] Z. Yang, F. Mikšík, K. Thu, T. Miyazaki, A Review on Development of Heat and Mass Transfer Enhancement in Adsorption Heat Exchangers, Proceedings of International Exchange and Innovation Conference on Engineering & Sciences (IEICES). 7 (2021) 240–246.

[4] B. Smith, T. Brunschwiler, B. Michel, Comparison of transient and static test methods for chip-to-sink thermal interface characterization, Microelectron. J. 40 (2009) 1379–1386.

[5] P.L. Kapitza, The study of heat transfer in helium ii, J. Phys. (USSR) 4 (1941) 181–210.

[6] E.T. Swartz, R.O. Pohl, Thermal boundary resistance, Rev. Mod. Phys. 61 (1989) 605–668.

[7] J. Pelzl, S. Chotikaprakhan, D. Dietzel, B.K. Bein, E. Neubauer, M. Chirtoc, The thermal contact problem in nano- and micro-scale.

[8] M.M. Yovanovich, Four decades of research on thermal contact, gap, and joint resistance in microelectronics, IEEE Trans. Compo. Pack. Technol. 28 (2005) 182–206.

[9] M. Asif, A. Tariq, Correlations of thermal contact conductance for nominally flat metallic contact in vacuum, Exp. Heat Transfer 29 (2016) 456–484.

[10] R. Dou, T. Ge, X. Liu, Z. Wen, Effects of contact pressure, interface temperature, and surface roughness on thermal contact conductance between stainless steel surfaces under atmosphere condition, Int. J. Heat Mass Transfer 94 (2016) 156–163.

[11] P.E. Hopkins, Thermal transport across solid interfaces with nanoscale imperfections: effects of roughness, disorder, dislocations, and bonding on thermal boundary conductance, ISRN Mech. Eng. 2013 (2013) 1–19.

[12] B.B. Mikic, Thermal contact conductance; Theoretical considerations, Int. J. Heat Mass Transfer 17 (1974) 205–214.

[13] M. Bahrami, M.M. Yovanovich, J.R. Culham, Thermal contact resistance at low contact pressure: effect of elastic deformation, Int. J. Heat Mass Transfer 48 (2005) 3284–3293.

[14] L.S. Fletcher, Recent developments in contact conductance heat transfer, J. Heat Transfer 110 (1988) 1059–1070.

[15] S. Zhai, P. Zhang, Y. Xian, J. Zeng, B. Shi, Effective thermal conductivity of polymer composites: theoretical models and simulation models, Int. J. Heat Mass Transfer 117 (2018) 358–374.

[16] G. Nagayama. Boundary conditions and microscale heat transfer at solid-liquid interface. J. Heat Transfer Soc. Jpn, 2011, 50(211): 29-36.

[17] G. Nagayama, P Cheng. Effects of interface wettability on microscale flow by molecular dynamics simulation, Int. J. Heat Mass Transfer, (2004), 501-513.

[18] B. Sponagle, D. Groulx, Measurement of thermal interface conductance at variable clamping pressures using a steady state method, Appl. Therm. Eng. 96 (2016) 671–681.

[19] D. Liu, Y. Luo, X. Shang, Experimental investigation of high temperature thermal contact resistance between high thermal conductivity c/c material and inconel 600, Int. J. Heat Mass Transfer 80 (2015) 407–410.

[20] W. Zongren, Y. Jun, W. Shuang, Z. Weifang, Compensation heating technique for experimental investigation of thermal contact conductance across gh4169/k417 interface, Rare Metal Mat. Eng. 42 (2013) 1572–1575.

[21] C. Fieberg, R. Kneer, Determination of thermal contact resistance from transient temperature measurements, Int. J. Heat Mass Transfer 51 (2008) 1017–1023.

[22] K.R. McDonald, J.R. Dryden, A. Majumdar, F.W. Zok, A photothermal technique for the determination of the thermal conductance of interfaces and cracks, J. Heat Transfer 122 (2000) 10–14.

[23] Y. Ohsone, G. Wu, J. Dryden, F. Zok, A. Majumdar, Optical measurement of thermal contact conductance between wafer-like thin solid samples, J. Heat Transfer 121 (1999) 954–963.

[24] J. Zhu, D. Tang, W. Wang, J. Liu, K.W. Holub, R. Yang, Ultrafast thermoreflectance techniques for measuring thermal conductivity and interface thermal conductance of thin films, J. Appl. Phys. 108 (2010) 94315.

[25] A.J. Schmidt, R. Cheaito, M. Chiesa, Characterization of thin metal films via frequency-domain thermoreflectance, J. Appl. Phys. 107 (2010) 24908.

[26] Z. Chen, W. Jang, W. Bao, C.N. Lau, C. Dames, Thermal contact resistance between graphene and silicon dioxide, Appl. Phys. Lett. 95 (2009) 161910.

[27] J. Chen, W. Zhang, Z. Feng, W. Cai, Determination of thermal contact conductance between thin metal sheets of battery tabs, Int. J. Heat Mass Transfer 69 (2014) 473–480.

[28] N.D. Miloševic, Determination of transient thermal interface resistance between two bonded metal bodies using the laser-flash method, Int. J. Thermophys. 29 (2008) 2072–2087.

[29] R. N. Wenzel, RESISTANCE OF SOLID SURFACES TO WETTING BY WATER, Ind. Eng. Chem. 28 (1936) 988–994.

[30] A. B. D. Cassie, S. Baxter, Wettability of porous surfaces, Trans. Faraday Soc. 40 (1944) 546.

[31] G. Nagayama, D. Zhang, Intermediate wetting state at nano/microstructured surfaces, Soft Matter. 16 (2020) 3514–3521.

[32] ASTM D5470-06, Standard test method for thermal transmission properties of thermally conductive electrical insulation materials, America: ASTM International, 2006.

[33] C. Fieberg, R. Kneer, Determination of thermal contact resistance from transient temperature measurements, International Journal of Heat and Mass Transfer. 51 (2008) 1017–1023.

[34] Y. Jiao, K. Miyazaki, T. Yabuki, Measurement of thermal boundary resistance between water and superhydrophobic surfaces by the bi-directional differential 3ω method, International Communications in Heat and Mass Transfer. 126 (2021) 105404.

[35] J. Chen, W. Zhang, Z. Feng, W. Cai, Determination of thermal contact conductance between thin metal sheets of battery tabs, International Journal of Heat and Mass Transfer. 69 (2014) 473–480.

[36] E.M. Burghold, Y. Frekers, R. Kneer, Determination of time-dependent thermal contact conductance through IR-thermography, International Journal of Thermal Sciences. 98 (2015) 148–155.

[37] Z. Ge, D.G. Cahill, P.V. Braun, Thermal Conductance of Hydrophilic and Hydrophobic Interfaces, Phys. Rev. Lett. 96 (2006) 186101.

[38] H. Harikrishna, W.A. Ducker, S.T. Huxtable, The influence of interface bonding on thermal transport through solid–liquid interfaces, Appl. Phys. Lett. 102 (2013) 251606.

[39] A. Schmidt, M. Chiesa, X. Chen, G. Chen, An optical pump-probe technique for measuring the thermal conductivity of liquids, Review of Scientific Instruments. 79 (2008) 064902.

[40] Ira Y., Kodama T., Shiomi J., Reduction of interface thermal resistance between TIM and metal surface by tuning wettability, Transactions of the JSME (in Japanese). 87 (2021) 21-00023-21–00023.

[41] X. Wang, B.A. Cola, T.L. Bougher, S.L. Hodson, T.S. Fisher, X. Xu, PHOTOACOUSTIC TECHNIQUE FOR THERMAL CONDUCTIVITY AND THERMAL INTERFACE MEASUREMENTS, Annual Rev Heat Transfer. 16 (2013) 135–157.